

Characterization of temperature non-uniformity over a premixed CH₄–air flame based on line-of-sight TDLAS

Guangle Zhang¹ · Jianguo Liu¹ · Zhenyu Xu¹ · Yabai He¹ · Ruifeng Kan¹

Received: 19 August 2015 / Accepted: 12 November 2015 / Published online: 19 January 2016
© Springer-Verlag Berlin Heidelberg 2016

Abstract A novel technique for characterizing temperature non-uniformity has been investigated based on measurements of line-of-sight tunable diode laser absorption spectroscopy. It utilized two fiber-coupled distributed feedback diode lasers at wavelengths around 1339 and 1392 nm as light sources to probe the field at multiple absorptions lines of water vapor and applied a temperature binning strategy combined with Gauss–Seidel iteration method to explore the temperature non-uniformity of the field in one dimension. The technique has been applied to a McKenna burner, which produced a flat premixed laminar CH₄–air flame. The flame and its adjacent area formed an atmospheric field with significant non-uniformity of temperature and water vapor concentration. The effect of the number of temperature bins on column-density and temperature results has also been explored.

1 Introduction

As a noninvasive spectroscopic technology, tunable diode laser absorption spectroscopy (TDLAS) is nondestructive and environmentally friendly. It has high sensitivity and selectivity and permits fast, in situ absorption measurements to obtain related information about temperature,

concentration, pressure, velocity and mass flux of gases, as well as spectral features in liquid and solid phases [1]. Thanks to these advantages, TDLAS is favored in science and engineering disciplines such as bioscience [2], geological science [3], geophysics [4], pharmaceutical science [5, 6], chemical science [7, 8], atmospheric environmental monitoring [9–11], industrial process monitoring [12], medical diagnostics [13–15] and combustion diagnostics [16–18]. Among these fields, combustion diagnostics are in great need of a technique like TDLAS due to tough conditions of combustion fields. There are two key parameters, i.e., temperature and concentration of combustion products, to be measured in diagnoses because of their importance in determining combustion efficiency. These two parameters were usually obtained as averaged values along a laser beam path in a uniform field, or by assuming the measured fields were nearly uniform [19–21]. However, due to the effects of flow boundary layers, heat transfer between surfaces, flow mixing, inhomogeneous combustion zones, buoyancy and phase change, significant non-uniformities in temperature and species concentration exist in many practical flow fields. Many efforts were made to handle the non-uniformity. For example, Ouyang and Varghese proposed an energy–temperature curve method to correct for the thermal boundary layer effects which led to non-uniformity [22]. Wang et al. [23] found a way to reduce effects of the non-uniformities. Palaghita and Seitzman [24] correlated a pattern factor with the path-averaged temperatures inferred from different line pairs. Some tomographic reconstructions of laser absorptions were also demonstrated in laboratory experiments by using multiple optical beams to probe a measured field [25–27]. However, the redundancy of tomographic technique makes it unpopular in practical devices. So some researchers prefer LOS-TDLAS (line-of-sight tunable diode laser absorption spectroscopy), which can diagnose the

✉ Jianguo Liu
jgliu@aiofm.ac.cn

✉ Ruifeng Kan
kanruifeng@aiofm.ac.cn

Guangle Zhang
glzhang@aiofm.ac.cn

¹ Key Laboratory of Environmental Optics & Technology, Anhui Institute of Optics and Fine Mechanics, Chinese Academy of Sciences, Hefei 230031, China

non-uniformity of measured fields with only one optical beam. Sanders et al. demonstrated the use of LOS-TDLAS by using O₂ absorption lines [28], and so did Liu et al. with H₂O lines [29] and other predecessors [30].

In this paper, we report development and experimental demonstration of a novel technique for one-dimensional non-uniformity measurements. We applied LOS-TDLAS on multiple absorption lines, by using two DFB diode lasers at wavelengths near 1392 and 1339 nm, and combined data analysis with an attractive temperature binning strategy and a Gauss–Seidel iteration method. The theoretical principles and experimental details are presented in Sects. 2 and 3, followed by data analysis, results and discussions in Sects. 4 and 5, respectively. We also explored how the number of temperature bins affects the analysis performance.

2 Theoretical background

2.1 TDLAS for non-uniform field measurements

Our experimental LOS-TDLAS system was based on absorption measurements of an incident laser beam propagating through a target field. According to the Lambert–Beer law, a change in laser beam intensity over a short distance dx due to spectroscopic absorption can be described by following Eq. (1):

$$\frac{-dI(\nu)}{I(\nu)} = P \cdot \sum_{l=1}^K X_{abs,l}(x) \cdot \sum_{i=1}^{N_l} S_{i,l}(T(x)) \cdot \Phi_{i,l}(\nu - \nu_{i,l}) \cdot dx, \tag{1}$$

In the above formula, $I(\nu)$ is the intensity of laser beam of frequency ν ; P [atm] is the total pressure; $T(x)$ [K] is the local temperature at position x ; $X_{abs,l}(x)$ is the local mole fraction (or volume mixing ratio) of species l ; K is the total number of species; N_l is the total number of involved transitions of the species l ; $S_{i,l}$ [$\text{cm}^{-2} \cdot \text{atm}^{-1}$] and $\Phi_{i,l}$ [cm] are the line strength and line shape function with a center frequency $\nu_{i,l}$ for transition i of species l , respectively. The line strength of transition i of a species at temperature T can be calculated with the help of Eq. (2), based on the line strength at a reference temperature T_0 (usually 296 K) as listed in the HITRAN or HITEMP spectroscopic database [31]:

$$S_i(T) = S_i(T_0) \frac{Q(T_0)}{Q(T)} \left(\frac{T_0}{T}\right) \exp\left[-\frac{hcE_i''}{k} \left(\frac{1}{T} - \frac{1}{T_0}\right)\right] \times \left[1 - \exp\left(\frac{-hc\nu_i}{kT}\right)\right] \left[1 - \exp\left(\frac{-hc\nu_i}{kT_0}\right)\right]^{-1}, \tag{2}$$

where h [J s] is the Planck constant; c [cm/s] is the speed of light, k [J/K] is the Boltzmann constant; $Q(T)$ is the partition function of the species; ν_i [cm^{-1}] and E_i'' [cm^{-1}] are

the resonant frequency and lower state energy of the transition i , respectively.

With an integral of Eq. (1) going through the whole path length from 0 to L , and some deductions, the absorbance $\alpha(\nu)_{i,l}$ (at frequency ν , for a single transition i of species l) can be expressed by Eq. (3):

$$\alpha(\nu)_{i,l} = P \cdot \int_0^L X_{abs,l}(x) \cdot S_{i,l}(T(x)) \cdot \Phi_{i,l}(\nu - \nu_{i,l}) \cdot dx, \tag{3}$$

The line shape function $\Phi_{i,l}(\nu - \nu_{i,l})$ is normalized as $\int_{-\infty}^{+\infty} \Phi_{i,l}(\nu - \nu_{i,l}) \cdot d\nu \equiv 1$. So the integrated absorbance $A_{i,l}$ [cm^{-1}] for a single absorption line can be inferred from Eq. (3) as

$$A_{i,l} = \int_{-\infty}^{\infty} \alpha(\nu)_{i,l} d\nu = P \cdot \int_0^L X_{abs,l}(x) \cdot S_{i,l}(T(x)) \cdot dx. \tag{4}$$

2.2 Temperature binning strategy with Gauss–Seidel method

A temperature binning strategy was used for data processing. Here, we introduce it only briefly. Temperature binning means splitting the whole optical path into several (e.g., n) sections, each section j of which with a representative temperature T^j , an absorber mole fraction of X_{abs}^j and a path length of L^j . Then, Eq. (4) can be rewritten and reduced for the case of this study where only a single target absorber species (i.e., H₂O vapor) was involved, as

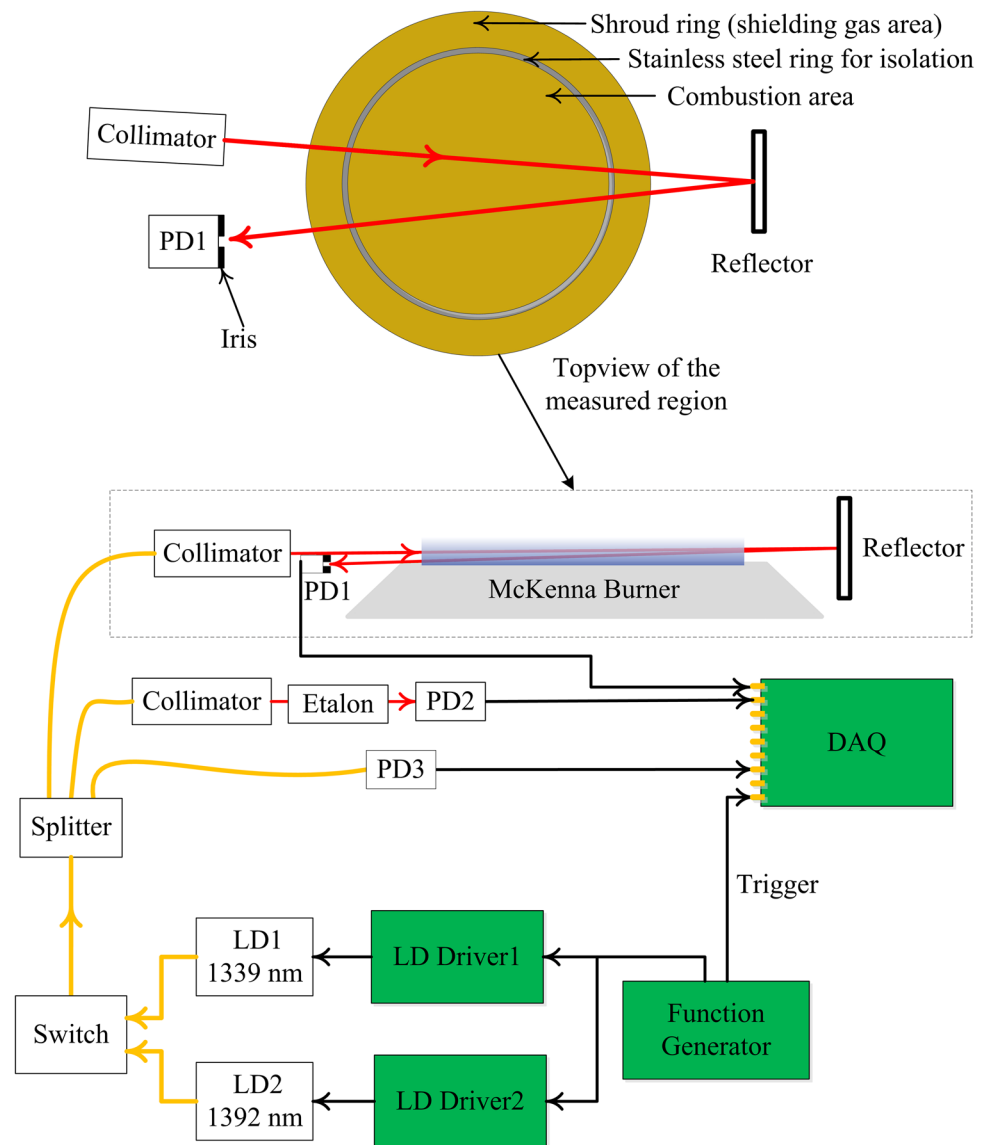
$$A_i = P \cdot \sum_{j=1}^n \left[S_i(T^j) \cdot X_{abs}^j \cdot L^j \right], \tag{5}$$

The product $X_{abs}^j \cdot L^j$ is referred here also as the column density CD^j of mole fraction of the target absorber in the section j . The mole fraction X_{abs} is non-dimensional, so the dimension of column density of mole fraction is the same as that of path length, i.e., cm. To solve Eq. (5), measurements of A_i for m (greater than or equal to n) absorption lines will be needed. These will then form the following linear equation set:

$$\begin{bmatrix} S_1(T^1) & S_1(T^2) & \cdots & S_1(T^n) \\ S_2(T^1) & S_2(T^2) & \cdots & S_2(T^n) \\ \vdots & \vdots & \vdots & \vdots \\ S_m(T^1) & S_m(T^2) & \cdots & S_m(T^n) \end{bmatrix} \cdot \begin{bmatrix} P \cdot X_{abs}^1 \cdot L^1 \\ P \cdot X_{abs}^2 \cdot L^2 \\ \vdots \\ P \cdot X_{abs}^n \cdot L^n \end{bmatrix} = \begin{bmatrix} A_1 \\ A_2 \\ \vdots \\ A_m \end{bmatrix}, \tag{6}$$

To obtain the column density of mole fraction, we took Gauss–Seidel iteration method to solve the above equation set. Gauss–Seidel iterative matrix is derived from the coefficient

Fig. 1 Schematic of the experimental setup. *PD* photodiode, *LD* laser diode, *DAQ* data acquisition



matrix (S), which is calculated based on Eq. (2) by adjusting and optimizing representative temperature T^j for each section j . The solutions of Eq. (6) for each product $X_{abs}^j \cdot L^j$ represent the corresponding quantity of column density CD^j of mole fraction. When applying Eq. (6) to analyze experimental measurements, we verified the convergence of the iterative matrix and the results' independence from their coarse initial input values. The selection of absorption lines to be measured affects the convergence characteristics of the Gauss–Seidel iterative matrix as we have reported. The selection of wavelengths in this study was limited by the availability of our laser sources.

3 Experimental details

A schematic diagram of the experimental apparatus is shown in Fig. 1. Two fiber-coupled DFB diode lasers (Nanoplus)

equipped with optical isolators operated at wavelengths around 1339 and 1392 nm, respectively. Their operation temperatures and currents were driven by two controllers (Thorlabs ITC102). Operation currents of both lasers were rapidly modulated with a sawtooth waveform with a period of 1.2 ms produced by a function generator. Consequently, the wavelength of the 1339-nm diode laser was rapidly scanned over 0.5 nm ($\sim 2.9 \text{ cm}^{-1}$) by the sawtooth current modulation, whereas the wavelength of the 1392-nm diode laser was tuned over 1.3 nm ($\sim 7 \text{ cm}^{-1}$). Each diode laser covered several absorption lines of H₂O molecules. Table 1 lists details of all the absorption lines utilized in this study, which were obtained from the latest HITRAN spectroscopy database. Considering line 1a and line 1b are closely overlapping and have almost the same lower state energy, they were treated as a combined line with two line strengths added together and sharing the rest parameters of the stronger line. We repeated

Table 1 Characteristics of individual absorption lines of H₂O molecules

| Line number | Frequency, cm ⁻¹ | Wavelength, nm | Line strength at 296 K, cm ⁻¹ /(molecule cm ⁻²) | Lower state energy, cm ⁻¹ |
|-------------|-----------------------------|----------------|--|--------------------------------------|
| 1a | 7179.7522 | 1392.806 | 1.802E-22 | 1216.1945 |
| 1b | 7179.7534 | 1392.805 | 6.009E-23 | 1216.1897 |
| 2 | 7181.1558 | 1392.533 | 1.505E-20 | 136.7617 |
| 3a | 7185.5966 | 1391.673 | 1.995E-22 | 1045.0583 |
| 3b | 7185.5969 | 1391.673 | 5.984E-22 | 1045.0577 |
| 4a | 7465.9000 | 1339.423 | 1.193E-25 | 2631.2822 |
| 4b | 7465.9120 | 1339.421 | 3.579E-25 | 2631.2671 |
| 5a | 7466.3356 | 1339.345 | 1.178E-25 | 2660.9448 |
| 5b | 7466.3361 | 1339.345 | 3.532E-25 | 2660.9441 |
| 6 | 7467.7689 | 1339.088 | 5.123E-25 | 2551.4834 |

Based on the spectral database HITRAN <https://www.cfa.harvard.edu/hitran/>

Table 2 Characteristics of effectively combined absorption lines of H₂O molecules

| Line number | Frequency, cm ⁻¹ | Wavelength, nm | Line strength at 296 K, cm ⁻¹ /(molecule cm ⁻²) | Lower state energy, cm ⁻¹ |
|-------------|-----------------------------|----------------|--|--------------------------------------|
| 1 | 7179.7522 | 1392.806 | 2.4029E-22 | 1216.1945 |
| 2 | 7181.1558 | 1392.533 | 1.505E-20 | 136.7617 |
| 3 | 7185.5969 | 1391.673 | 7.979E-22 | 1045.0577 |
| 4 | 7465.9120 | 1339.421 | 4.772E-25 | 2631.2671 |
| 5 | 7466.3361 | 1339.345 | 4.710E-25 | 2660.9441 |
| 6 | 7467.7689 | 1339.088 | 5.123E-25 | 2551.4834 |

similar treatments for lines 3a and 3b, lines 4a and 4b and lines 5a and 5b. Based on theoretical calculations, this grouping process had no effect on our final results but simplified data processing. The final effective spectroscopic line information used in this paper for measurement data processing is listed in Table 2.

Laser output radiation was divided by a fiber optic splitter into multiple beams. One beam was collimated and passed through the target flame field to measure the absorption signal. A second laser beam was coupled into an etalon generating an interference signal for calibrations of laser wavelength scans. A plane mirror placed near the McKenna burner enabled a double-path arrangement for the flame measurement beam to enhance the absorption. The total length of the measurement path was 258 mm, of which the combustion section was 118 mm long and the rest was ambient air (apart from an 11-mm thin layer of nitrogen shielding gas). Laser beam intensities were detected by photodetectors and recorded by a data acquisition (DAQ) card (NI PXI-5105) for data analysis. To enhance the signal-to-noise ratio, averaged spectral measurement scans were used and analyzed usually. Such a set of measurements at both the 1339-nm and the 1392-nm regions are shown in Fig. 2.

The McKenna burner used in the experiment was a standard water-cooled bronze burner with a bronze shroud ring surface area for shielding gas flow, produced by the company Holthuis & Associates. A diagram of the burner's top view is shown in Fig. 1. The combustion area was a sintered bronze disk with a diameter of 60 mm. The shielding gas area was a sintered bronze shroud ring with an outside diameter of 73.5 mm and an inside diameter of 62.6 mm. The gas flows to these two areas were isolated by an internal stainless steel ring structure between them. In this demonstration study, methane and dry air were premixed and supplied to the burner with flow rates of 1.35 slpm (standard liter per min) and 12.8 slpm, respectively. High-purity nitrogen flowed at a rate of 5.8 slpm through a purge slot into the shroud ring to prevent the formation of end flames [32]. The gas flow rates were controlled by three SLA5850 mass flow controllers produced by Brooks Instrument. The probe laser beam propagated through the flame field at a height of 4 mm above the sintered bronze disk. The absorption spectra at the two wavelength regions were measured successively by switching from one laser to another laser. Considering the little time difference, the flame field underwent no significant changes between the two absorption spectra measurements.

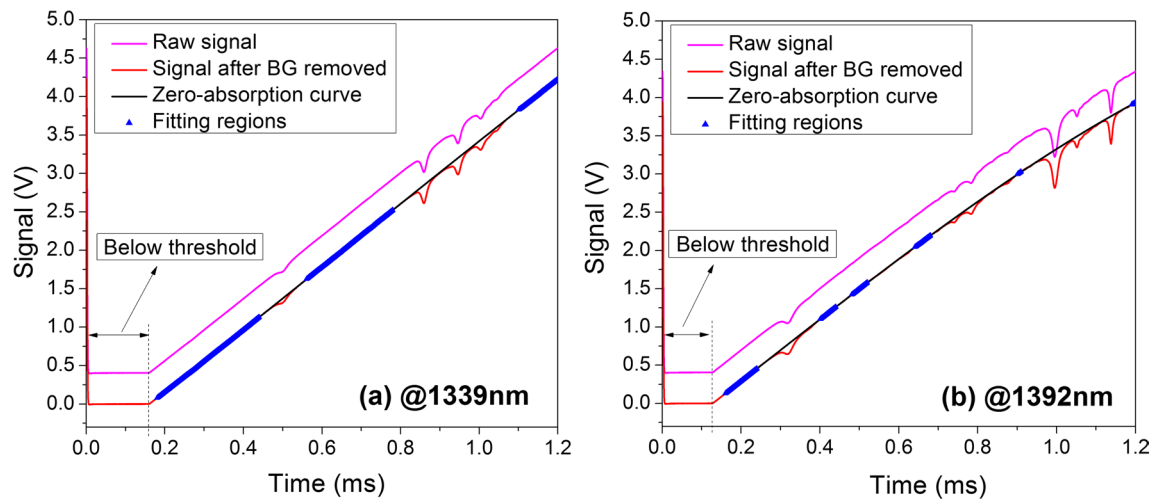
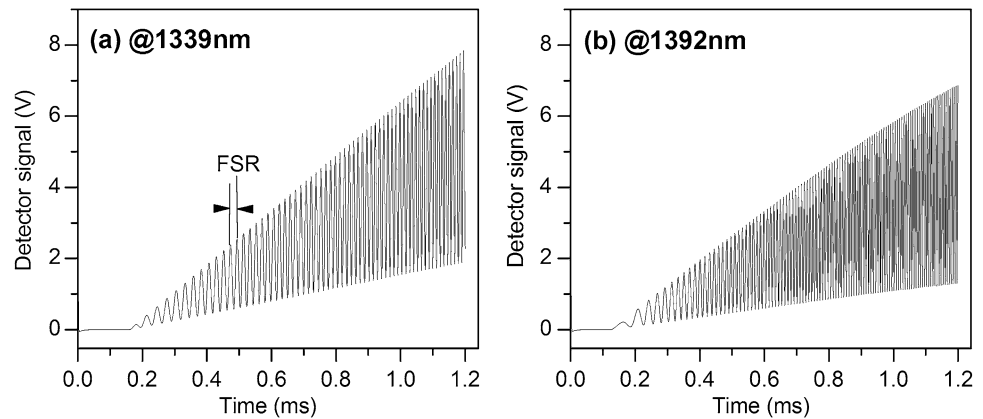


Fig. 2 Raw H₂O spectral measurement signals and the processed results showing the first two processing steps (removal of background offset and determination of zero-absorption intensity curve)

Fig. 3 Etalon interference signals showing wavelength scans of both diode lasers as their operation currents were modulated with a sawtooth waveform



4 Data processing

For spectroscopic data analyses, firstly, we removed background signal of the photodetector output by subtracting the photodetector output with its offset value when the corresponding laser current was below its operation threshold, as shown in Fig. 2. Below laser current threshold, the photodetector registered no spectroscopic information, only room lights, flame emission and other background noise. Secondly, the zero-absorption intensity profiles were obtained by a third-order polynomial fit to the regions without absorption. As displayed in Fig. 2, the polynomial fits of zero-absorption intensity profiles matched the overall measurements quite well.

Thirdly, we obtained the absorbance $\alpha(\nu)$ by calculating the natural algorithm of the ratio of zero-absorption intensity to transmitted laser intensity. Fourthly, the etalon interference signals (shown in Fig. 3) were processed to determine the scanned wavelength. A set of example

spectra obtained after these processing steps are displayed in Fig. 4. Fifthly, we performed a Voigt profile fit to each of the absorption lines to obtain their integrated absorbance A_i . Finally, the column densities were computed with different numbers of temperature bins by using the Gauss–Seidel iteration method as described in Sect. 2. Four different values for the number of temperature bins, with $n = 3, 4, 5$ and 6 , respectively, were tested to investigate its effect on the temperature non-uniformity estimations. Typically, 30 sets of absorbance measurements were processed for both the three absorption lines around 1339 nm and the three lines around 1392 nm.

The performance of this temperature non-uniformity analysis technique was evaluated by two parameters: RMS_STDs (the root mean square of the sample standard deviations STD^j of multiple sets of measurements of the column-density values of each temperature bin) and RMS_REs (the root mean square of residual errors between the measurement average and the expected column-density results over

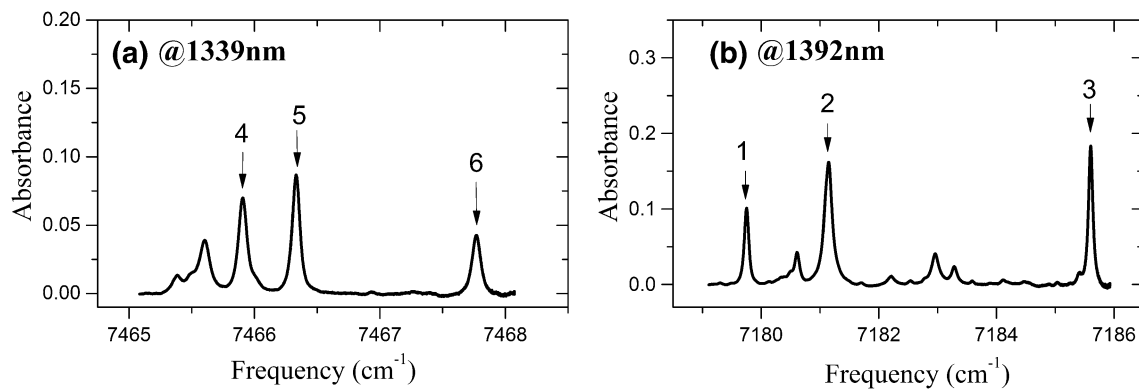


Fig. 4 Absorption spectra of measurements at both wavelength regions with two DFB diode lasers. Six H₂O lines are labeled with the corresponding line number as listed in Table 2

all temperature bins). The expected column-density values are explained in Sect. 5. These two parameters are defined by Eqs. (8) and (9), respectively. CD_{expected}^j is the expected column density of each bin; CD_{measured}^j is the averaged measurement column density of each bin. The sample standard deviation STD^j and mean column-density value at each temperature bin j , for a typical 30 sets of measurements, are defined by Eqs. (10) and (11), respectively.

$$\text{RMS_STDs} = \sqrt{\frac{\sum_{j=0}^n (STD^j)^2}{n}}, \quad (7)$$

$$\text{RMS_REs} = \sqrt{\frac{\sum_{j=0}^n \left(CD_{\text{measured}}^j - CD_{\text{expected}}^j \right)^2}{n}}, \quad (8)$$

$$STD^j = \sqrt{\frac{\sum_{k=1}^{30} \left| CD_{\text{measured},k}^j - \overline{CD_{\text{measured},k}^j} \right|^2}{30 - 1}}, \quad (9)$$

$$\overline{CD_{\text{measured}}^j} = \frac{\sum_{k=1}^{30} CD_{\text{measured},k}^j}{30}. \quad (10)$$

5 Results and discussion

The temperature at the center of the combustion area was measured independently with a B-type thermocouple placed at the same height as the laser beam above the burner plate to be about 1535 K, whereas the temperature range of the surrounding room air was obtained with a K-type thermocouple moving through the measured path to be about 300–313 K. We set the temperature bins evenly between 300 and 1535 K. The flat premixed laminar flame produced under the conditions mentioned in Sect. 3 was very stable and uniform due to accurate flow rate control and nitrogen gas

shielding. Therefore, the column densities were expected to be zero at all other temperature bins except the 300-K bin and 1535-K bin. And these expected values also serve as starting point for the iteration. The final measurement and analysis results are presented in Figs. 5 and 7. Figure 5 depicts different column-density distributions as a function of different numbers of temperature bins $n = 3, 4, 5, 6$. The major component was always at the hottest temperature bin of 1535 K. Based on the analysis, the column density in the hottest bin is much higher than that in the coldest bin. This characteristic can be explained as follows. As described in Sect. 3, we know that the path length of the hot combustion section is 118 mm long, the total length of the nitrogen shielding gas layer is 44 mm, and the ambient-air section is 96 mm long. Through chemical and phase equilibrium calculation using CHEMKIN (a chemical calculation software from the company Reaction Design), the mole fraction of water vapor in the combustion section under a constant pressure and adiabatic condition was 0.184, whereas the mole fraction of water vapor in the ambient-air section had a much lower value of 0.0054, which was obtained based on room-temperature absorption measurements of the 7181.1558-cm⁻¹ line. This explains why the column density in the hottest bin is much higher than that in the coldest bin.

We verified the column-density results by dividing themselves by the corresponding mole fractions of water vapor. Taking three-bin results as an example, the column densities at the 300- and 1535-K bins were 0.0252 and 2.084 cm, respectively. Dividing them by their corresponding mole fraction values of 0.0054 and 0.184, the calculated lengths of the 300-K bin and of the 1535-K bin were 47 and 113 mm, respectively. The results indicated 49 % of the ambient-air section was at the temperature of 300 K and 95 % of the combustion section was at the temperature of 1535 K. To explore the large 49 % deviation for the length of the 300-K bin from its physical length of the ambient-air section, data were analyzed as follows. The value of the

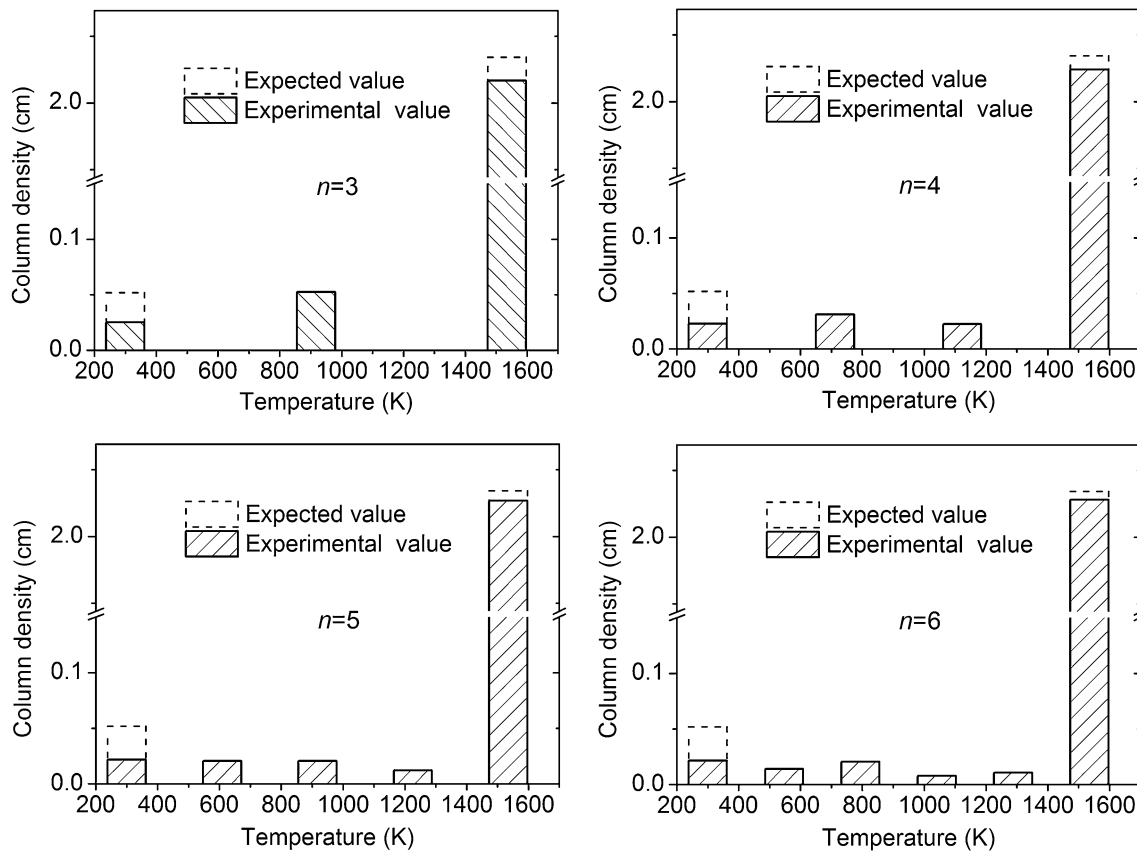


Fig. 5 Histogram of column density versus temperature bins, for four different total number of bins $n = 3, 4, 5$ and 6 , respectively. The expected values at 300 and 1535 K were based on a model calcula-

tion. The experimental values were based on analysis of experimental spectroscopic measurements

lowest temperature bin was changed from 290 to 320 K to observe its effect on the length results. As its temperature increased, the length result of ambient-air section increased by 5 %, whereas the length result of the combustion section decreased by 0.1 %. A similar analysis was undertaken for the effect of the value of the highest temperature bin on the length results. The length results of both sections increased by 1 % as the temperature was elevated from 1520 to 1550 K. This demonstrated that the temperature dependence of length estimation is more sensitive at room temperature (~ 300 K) than at high temperatures (~ 1500 K). This could be explained by the temperature characteristic of line strengths of selected lines shown in Fig. 6. As plotted, line 2 has much higher line strength and temperature sensitivity at temperatures below ~ 800 K. It should also be noted that the integrated absorbance of line 2 was obtained by fitting measured absorption spectra having 5 absorption lines including line 2. Significant interferences among these spectral lines made it difficult to determine the integrated absorbance accurately. Therefore, the estimated length result (47 mm) for ambient-air section was much lower than the corresponding setup length (96 mm) and

was compensated by estimated distributions at other temperature bins between the lowest and highest temperatures. Also, by changing the whole temperature range we discovered that a reasonable temperature range played a significant role in achieving reasonable measured results. Therefore, some prior knowledge about the temperature range was important. The selection of wavelengths in this study was not ideal, but limited by the availability of our laser sources. It would be beneficial if the lower state energies of selected lines could distribute evenly over a large range.

Figure 7 illustrates the dependence of analysis performance on different numbers of temperature bins, based on measurements of the six absorption lines. The two evaluation parameters, RMS_STDs and RMS_REs, decreased as total number of temperature bins (represented by n) increased. This gave us a hint that with this Gauss-Seidel iteration method we could separate the rough temperature range into more bins to get more information about temperature field with improved analysis performance. To test the reliability of the method, we conducted comprehensive verifications based on computer simulations [33] and arrived at the conclusion that the method we used is reliable.

Fig. 6 Temperature characteristics of the line strengths of the selected H₂O lines

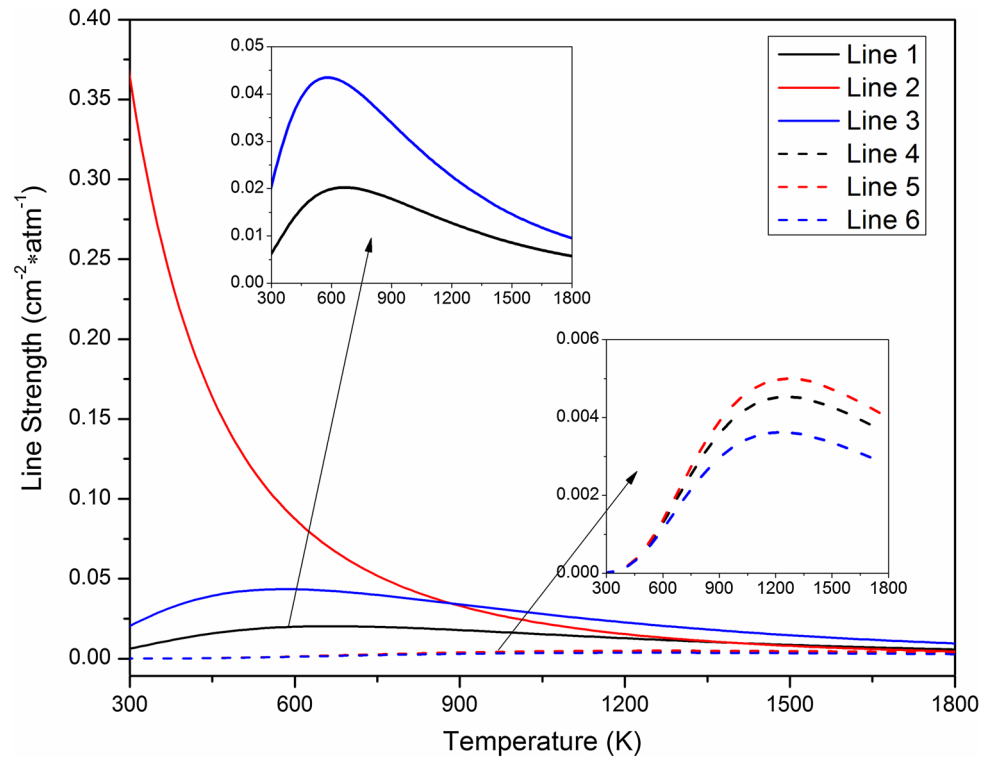
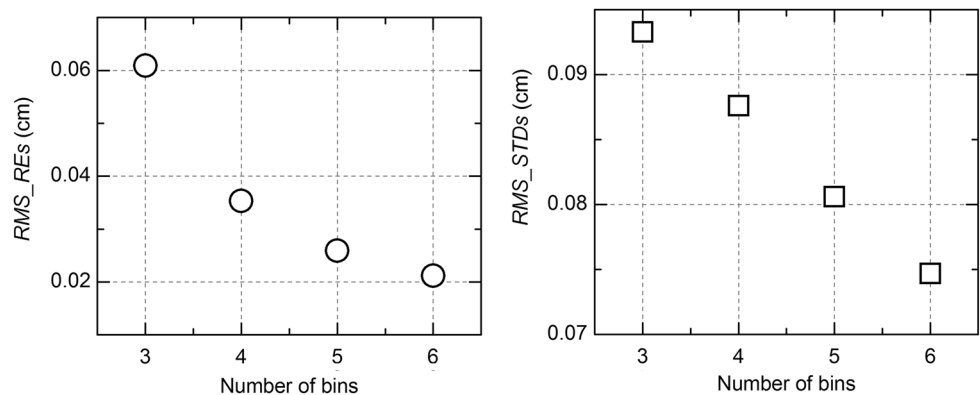


Fig. 7 Trends of the two evaluation parameters as a function of different numbers of temperature bins



However, as mentioned already in Sect. 2, the convergence characteristics of the Gauss–Seidel iterative matrix depend on the absorption lines used.

6 Conclusion

One-dimensional temperature non-uniformity measurements were well demonstrated by a novel LOS-TDLAS technique using two DFB diode lasers, one at wavelength near 1339 nm and the other near 1392 nm to measure absorption spectra of H₂O molecules and their temperature dependences. Reliable results were obtained through rigorous data processing with a temperature binning strategy

combined with Gauss–Seidel iterative method. This method provides enhanced temperature information by dividing temperature range into more bins. However, more bins require measurements of more absorption lines, and more absorption lines would require more compact diode lasers or more complex light sources. Fortunately, based on analysis with 3 or 4 temperature bins, the results obtained were good enough to present the temperature non-uniformity and water vapor concentration along the measured path in our experiment where the temperature of combustion section was quite uniform. For future research, we will consider using an external cavity diode laser (ECDL) as a light source, which could provide more flexibility in the selection of different absorption lines and wavelength scan range.

Acknowledgments This work was supported by the National Key Basic Research Program of China (973 Program) (Grant No. 2013CB632803), the National Key Scientific Instrument and Equipment Development Project of China (Grant No. 2014YQ060537) and the Youth Innovation Promotion Association of Chinese Academy of Sciences (Funding No. 2013208).

References

- J.S. Li, B.L. Yu, W.X. Zhao, W.D. Chen, *Appl. Spectrosc. Rev.* **49**, 666–691 (2014)
- S. Hunsmann, K. Wunderle, S. Wagner, U. Rascher, U. Schurr, V. Ebert, *Appl. Phys. B* **92**, 393–401 (2008)
- G. Durry, J.S. Li, I. Vinogradov, A. Titov, L. Joly, J. Cousin, T. Decarpenterie, N. Amarouche, X. Liu, B. Parvitte, O. Korablev, M. Gerasimov, V. Zéninari, *Appl. Phys. B* **99**, 339–351 (2010)
- T. Schilling, F.J. Lübken, F.G. Wienhold, P. Hoor, H. Fischer, *Geophys. Res. Lett.* **26**, 303–306 (1999)
- W.Y. Kuu, S.L. Nail, G. Sacha, *J. Pharm. Sci.* **98**, 1136–1154 (2009)
- W.Y. Kuu, K.R. O’Bryan, L.M. Hardwick, T.W. Paul, *Pharm. Dev. Technol.* **16**, 343–357 (2011)
- G.W. Harris, D. Klemp, T. Zenker, *J. Atmos. Chem.* **15**, 327–332 (1992)
- Y. Fujii, S. Tsushima, S. Hirai, *J. Therm. Sci. Tech.* **3**, 94–102 (2008)
- A. Fried, B. Henry, B. Wert, S. Sewell, J.R. Drummond, *Appl. Phys. B* **67**, 317–330 (1998)
- T. Gardiner, M.I. Mead, S. Garcelon, R. Robinson, N. Swann, G.M. Hansford, P.T. Woods, R.L. Jones, *Rev. Sci. Instrum.* **81**, 083102 (2010)
- S. Kaierle, X. Lin, X.L. Yu, F. Li, S.H. Zhang, J.G. Xin, X.Y. Chang, J.R. Liu, J.L. Cao, *Proc. SPIE* **8796**, 87961J (2013)
- I. Linnerud, P. Kaspersen, T. Jæger, *Appl. Phys. B* **67**, 297–305 (1998)
- C. Roller, K. Namjou, J. Jeffers, *Opt. Lett.* **27**, 107–109 (2002)
- M. Lewander, Z.G. Guan, K. Svanberg, S. Svanberg, T. Svensson, *Opt. Express* **17**, 10849–10863 (2009)
- A. Hartmann, R. Strzoda, R. Schrobenauser, R. Weigel, *Appl. Phys. B* **116**, 1023–1026 (2014)
- T. I. Palaghita, J. M. Seitzman: “Absorption-based temperature-distribution-sensing for combustor diagnostics and control,” in *44th AIAA Aerospace Sciences Meeting and Exhibit*, (AIAA, 2006), 1–10
- S. Li, A. Farooq, R.K. Hanson, *Meas. Sci. Technol.* **22**, 125301–125311 (2011)
- S. Wagner, M. Klein, T. Kathrotia, U. Riedel, T. Kissel, A. Dreizler, V. Ebert, *Appl. Phys. B* **109**, 533–540 (2012)
- R.K. Hanson, P.K. Falcone, *Appl. Opt.* **17**, 2477–2480 (1978)
- J.T.C. Liu, G.B. Rieker, J.B. Jeffries, M.R. Gruber, C.D. Carter, T. Mathur, R.K. Hanson, *Appl. Opt.* **44**, 6701–6711 (2005)
- T. Cai, H. Jia, G. Wang, W. Chen, X. Gao, *Sensor Actuat A-Phys* **152**, 5–12 (2009)
- X. Ouyang, P.L. Varghese, *Appl. Opt.* **28**, 3979–3984 (1989)
- J. Wang, M. Maiorov, J.B. Jeffries, D.Z. Garbuzov, J.C. Connolly, R.K. Hanson, *Meas. Sci. Technol.* **11**, 1576–1584 (2000)
- T. I. Palaghita, J. M. Seitzman: “Pattern factor sensing and control based on diode laser absorption,” in *41st AIAA/ASME/SAE/ASEE Joint Propulsion Conference and Exhibit*, (AIAA, 2005), 1–12
- L. Ma, W. Cai, A.W. Caswell, T. Kraetschmer, S.T. Sanders, S. Roy, J.R. Gord, *Opt. Express* **17**, 8602–8613 (2009)
- V.L. Kasyutich, P.A. Martin, *Appl. Phys. B* **102**, 149–162 (2010)
- J.W. Lv, T. Zhou, H.B. Yao, *Proc. SPIE* **8905**, 89050Z (2013)
- S.T. Sanders, J. Wang, J.B. Jeffries, R.K. Hanson, *Appl. Opt.* **40**, 4404–4415 (2001)
- X. Liu, J.B. Jeffries, R.K. Hanson, *AIAA J.* **45**, 411–419 (2007)
- C. Liu, L. Xu, Z. Cao, *Appl. Opt.* **52**, 4827–4842 (2013)
- L.S. Rothman, I.E. Gordon, Y. Babikov, A. Barbe, D. Chris Benner, P.F. Bernath, M. Birk, L. Bizzocchi, V. Boudon, L.R. Brown, A. Campargue, K. Chance, E.A. Cohen, L.H. Coudert, V.M. Devi, B.J. Drouin, A. Fayt, J.M. Flaud, R.R. Gamache, J.J. Harrison, J.M. Hartmann, C. Hill, J.T. Hodges, D. Jacquemart, A. Jolly, J. Lamouroux, R.J. Le Roy, G. Li, D.A. Long, O.M. Lyulin, C.J. Mackie, S.T. Massie, S. Mikhailenko, H.S.P. Müller, O.V. Naumenko, A.V. Nikitin, J. Orphal, V. Perevalov, A. Perrin, E.R. Polovtseva, C. Richard, M.A.H. Smith, E. Starikova, K. Sung, S. Tashkun, J. Tennyson, G.C. Toon, V.G. Tyuterev, G. Wagner, *J. Quant. Spectrosc. Radiat. Transfer* **130**, 4–50 (2013)
- S. Wagner, B.T. Fisher, J.W. Fleming, V. Ebert, *Proc. Combust. Inst.* **32**, 839–846 (2009)
- G.L. Zhang, J.G. Liu, R.F. Kan, Z.Y. Xu, *Chin. Phys. B* **23**, 124207 (2014)